

Scientific paper

An Innovative Hybrid 3D Analytic-numerical Model for Air Breathing Parallel Channel Counter-flow PEM Fuel Cells

Gregor Tavčar* and Tomaž Katrašnik

University of Ljubljana, Faculty of Mechanical Engineering, Aškerčeva 6, SI-1000 Ljubljana, Slovenia

* Corresponding author: E-mail: gregor.tavcar@fs.uni-lj.si
Tel.: +386-1-4771-310; Fax: +386-1-2518-567

Received: 11-03-2014

Paper based on a presentation at the 4th RSE-SEE 2013 Symposium
on Electrochemistry in Ljubljana, Slovenia

Abstract

The parallel straight channel PEM fuel cell model presented in this paper extends the innovative hybrid 3D analytic-numerical (HAN) approach previously published by the authors with capabilities to address ternary diffusion systems and counter-flow configurations. The model's core principle is modelling species transport by obtaining a 2D analytic solution for species concentration distribution in the plane perpendicular to the channel gas-flow and coupling consecutive 2D solutions by means of a 1D numerical pipe-flow model. Electrochemical and other nonlinear phenomena are coupled to the species transport by a routine that uses derivative approximation with prediction-iteration. The latter is also the core of the counter-flow computation algorithm. A HAN model of a laboratory test fuel cell is presented and evaluated against a professional 3D CFD simulation tool showing very good agreement between results of the presented model and those of the CFD simulation. Furthermore, high accuracy results are achieved at moderate computational times, which is owed to the semi-analytic nature and to the efficient computational coupling of electrochemical kinetics and species transport.

Keywords: Fuel cells; species transport; electrochemical kinetics; analytic modelling; numerical modelling

1. Introduction

Proton Exchange Membrane fuel cells (PEMFC) are a power source featuring two major advantages: high power density and zero tank-to-wheel emissions. The analysis of Hellman and van der Hoed shows that the commercialization of PEM fuel cell technology is rather slow,¹ which is owed to several disadvantages characteristic to all fuel cell types, summarised by Ly et. al. as:² complexity and consequent cost, immaturity, and its role as replacement technology. In line with these facts Ly et. al. call for increased application of advanced mathematical modelling and simulation tools to efficiently address and tackle the shortcomings of the contemporary fuel cell technology.³

1. 1. Approaches to Fuel Cell Modelling

Physical processes in PEMFC comprise fully inter-

related mechanisms of convection, diffusion, phase transition and electrochemical reactions driving the transports of mass, charge and heat. Many fuel cell models can be found in literature or are available as packages in commercial software.^{3–5} They vary in the description of the physical phenomena, i.e. they address processes in PEMFC either analytically, mechanistically, semi empirically or fully empirically.

The non-empirical models can be further categorised according to the dimensionality of their description of the physical phenomena, i.e.: 0D,^{6–8} 1D,^{9–12} 2D,^{13–15} and 3D.^{16–22} In addition to these there are also intermediate models, commonly referred to as the reduced dimensionality models, which are models that do not address all modelled dimensions equally; i.e.: quasi 3D, 2D+1D, quasi 2D, and 1D + 1D models.^{23–29} The higher the dimensionality of a model the higher is the accuracy of its results but also the longer are its computational times.

Contrary to the non-empirical models the empirical models, i.e. data driven models, are both accurate and computationally fast. However, they lack any predictability and typically perform poorly at operational points beyond the field of calibration, since they are always characteristic to only one specific system and its performance data, which must be either measured or simulated using a different simulation tool.^{30,31,40,41}

As summarised in the article of Tavčar and Katrašnik (ref:²⁸) there is a large number of fuel cell simulating scenarios where model generality and short computational times are required.^{32–39} The requirement of model generality rules out the empirical models (i.e. data driven) while the need for short computational times calls for sacrifice in accuracy. The reduced dimensionality models have shown to offer the best compromises between accuracy and computational speed.²⁸

1. 2. HAN Reduced Dimensionality Model

Articles of Tavčar and Katrašnik propose an innovative Hybrid 3D Analytic Numerical approach to modelling species transport (HAN) in a PEM fuel cell as a way to obtain results with full 3D resolution whilst achieving short computational times.^{28,29} The principles of HAN modelling in those refs are presented on a straight channel co-flow fuel cell and its core principle can be summarized as:

- A hybrid 3D model constructed by taking a 1D numerical model for the gas-flow along the channel with a superimposed 2D analytic solution for the plane perpendicular to the gas-flow.
- The additional computational load introduced by the calculation of the 2D analytic solution was shown to be of the same order of magnitude as the computational load of the base 1D calculation proving this hybrid 3D approach to be computationally efficient.

The isothermal HAN models in refs:^{28,29} both assume co-flow configuration and exclusively binary gas mixtures (i.e. either oxygen and water vapour or hydrogen and water vapour). The isothermal HAN model presented in this paper is based on the mathematical formalism derived in refs:^{28,29} and extends this formalism to enable also:

- addressing ternary gas mixtures (i.e. cathode fed with air comprising oxygen, nitrogen and water vapour)
- simulating counter-flow configurations.

The modelling assumptions and the geometry of the modelled fuel cell are described in section 2; governing equations of the species transport and electrochemical reactions are given in section 3; the HAN approach to solving these governing equations is explained in section 4. The accuracy of HAN is evaluated by comparing the results on the polarisation characteristics and the results on the 3D distribution of physical variables obtained by

HAN with the ones obtained by a professional 3D CFD tool. The simulation setup is described in section 5; results and their analysis are given for both operational cases in section 6; and section 7 summarizes the main conclusions.

2. Model Assumptions and Geometry

The modelled fuel cell is a straight hydrogen-air type PEM fuel cell (FC) with its geometry taken from a laboratory test fuel cell operated in counter-flow configuration. The fuel cell topology and geometry are illustrated in Figure 1 (a) distinguishing the following sub-elements: the cathode feed part comprising cathode channels and cathode gas diffusion layer (GDL); a thin catalyst layer for oxygen reduction; a hydrated proton exchange membrane; a thin catalyst layer for hydrogen oxidation; anode feed part comprising anode channels and anode gas diffusion layer (GDL). Due to the symmetric geometry of the modelled fuel cell and the assumed isothermal operating conditions the modelling of the whole fuel cell is reduced onto modelling the fuel cell's representative unit which is a half of one rib, as depicted in Figure 1b.

The derivation of HAN mathematical model is based on four sets of assumptions: 1) regarding gaseous species transport, 2) regarding species transport across membrane and 3) regarding electrochemical reaction kinetics. Except for the ternary diffusion system on the cathode side the assumptions summarised below are the same as those used in the paper of Tavčar and Katrašnik.²⁸

The general assumptions are:

- I. A steady state solution of the problem is sought.
- II. The problem is isothermal, i.e. a constant uniform temperature is assumed for the whole fuel cell and no energy equation is calculated.

The assumptions regarding gaseous species transport are:

- III. All species in the channels and GDLs are gaseous and treated as ideal gas.
- IV. Constant gas pressure is assumed in gas equations and the gas flow is assumed incompressible throughout the fuel cell.
- V. The diffusion system is bi-componential at the anode (hydrogen and water vapour) and tri-componential at the cathode (oxygen, nitrogen and water vapour).
- VI. The effective (macroscopic) diffusion constant assumed in GDL is the diffusion constant for free space (which applies in the channel) divided by the tortuosity of the GDL.
- VII. Diffusion in gas in the direction of channel gas-flow is neglected.
- VIII. In the GDLs there is no convective transport in the direction of channel gas flow.
- IX. The gas flow in channels is laminar.

The assumptions regarding membrane species transport are:

- X. There is no gas crossover in the membrane.
- XI. At a given point in membrane the mobility of both water molecules and protons (in form of hydronium ions) is linearly proportional to the membrane water content at that point.
- XII. Within the membrane the species transport only occurs in the direction perpendicular to the membrane sheet.
- XIII. The average number of water molecules transported electro-osmotically by each proton is an independent constant.
- XIV. The concentration of mobile protons is constant throughout the whole membrane.
- XV. At the membrane/gas boundary the membrane water content is in equilibrium with the water vapour concentration in the gas.

The assumptions regarding electrochemical reactions are:

- XVI. Only electrochemical kinetics on the cathode catalyst is considered.
- XVII. The catalyst layers are infinitely thin and characterised by an effective surface exchange current density as current per unit area [A/m^2].
- XVIII. The electrical resistance of the GDLs is neglected and uniform constant electrical potential is assumed within the whole GDL for each of the two GDLs.

All the above assumptions follow the assumptions made by the other reduced dimensionality models mentioned in the introduction.

3. Governing Equations

This section summarises the governing equations given in ref.²⁸ and gives a detailed derivation of the tri-componential diffusion that is not covered in ref.²⁸. In section 4 these governing equations are solved for the fuel cell geometry presented in section 2 using the hybrid analytic numerical approach. Two sets of governing equations are distinguished: a set of governing equations dealing with species transport and a set dealing with electrochemical processes.

3. 1. Species Transport

Species transport in a PEM fuel cell takes place in three distinctive regions: the membrane, the gas diffusion layer (GDL) and the channel. According to assumptions X only transport of absorbed liquid water and aqueous solution of protons is considered in the membrane; in the GDLs and channels the transport of the reactant species (oxygen on the cathode side and hydrogen on the anode side), the spectator species (e.g. nitrogen) and the product species, i.e. water vapour, takes place in gaseous phase.

3. 1. 1. Species Transport Across Membrane

The model addresses the transport of the absorbed liquid water in the membrane and the transport of protons in form of hydronium ions across the membrane. Since the governing equations for the one dimensional (assumption XII) species transport in the membrane derived in the paper of Tavčar and Kutrašnik (ref.²⁸) fully apply to the case in the present paper the following two equations for

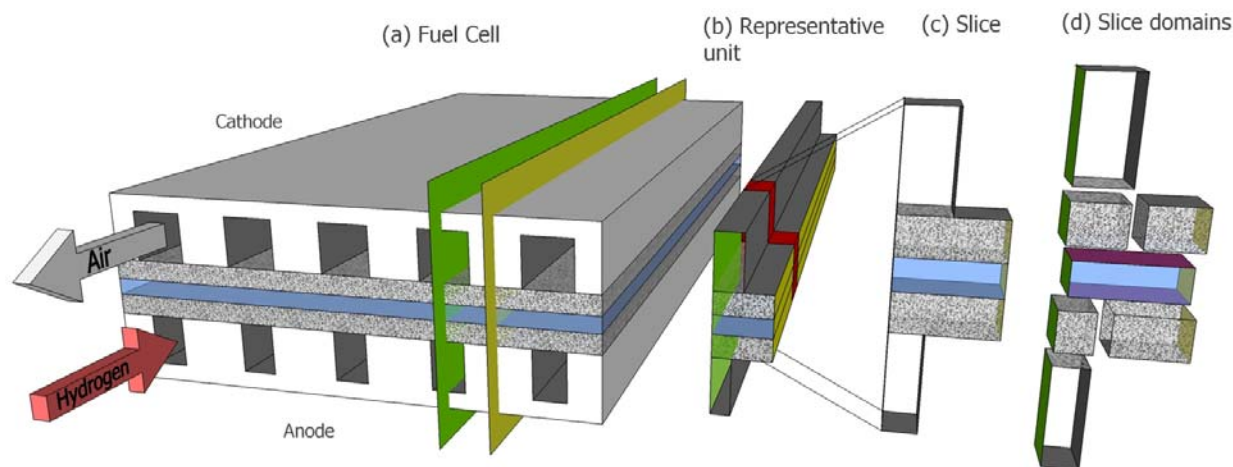


Figure 1 Fuel cell geometry schematically broken-down into elementary units for HAN computation. The blue regions represent the membrane and the spotted translucent the GDLs; the green surfaces represent the rib symmetry plane and the yellowish surfaces the symmetry plane between two ribs. (a) A five-rib parallel channel counter-flow fuel cell geometry. The two symmetry planes that apply to all ribs are shown delimiting the right half of one rib and so defining the representative unit. (b) Representative unit with one slice (red) indicated. (c) Slice as a sliced-out section of the representative unit. A slice has sufficiently small depth to be treated as a 2D object. (d) Slice split onto computational domains. Domains from top to bottom: cathode channel domain, two cathode GDL domains (left cathode GDL#1, right cathode GDL#2), MEA domain, two anode GDL domains (left anode GDL#1, right anode GDL#2), anode channel domain.

water and proton transport across the membrane summarise the comprehensive derivation in that paper.²⁸ Molar flux of water across the membrane is given by:

$$j_w = \frac{\mathfrak{D}_w}{2\vartheta} (\Lambda_{AND}^2 - \Lambda_{CTH}^2) + \frac{n_{drg}}{F} i, \quad (1)$$

where j_w is the molar fluxes of water across the membrane, Λ_{CTH} and Λ_{AND} are the water content Λ (i.e. concentration of water normalised with the sulphonic group concentration) at the MEA/GDL interface on the cathode and anode side respectively, n_{drg} is the electroosmotic drag coefficient, \mathfrak{D}_w is the coefficients of linear proportionality between the membrane water diffusion constant D_w and the membrane water content Λ (i.e. $D_w(\Lambda) = \mathfrak{D}_w \Lambda$), F is the Faraday constant, ϑ is the membrane thickness and i the current density. The specific ohmic resistance R of proton transport across the membrane reads:

$$R = \frac{2\vartheta RT}{F^2 \mathfrak{D}_+ c_+ (\Lambda_{AND} + \Lambda_{CTH})} \quad (2)$$

where \mathfrak{D}_+ is the coefficients of linear proportionality between the membrane proton diffusion constant D_+ (i.e. diffusion constant of hydronium H_3O^+ ions in membrane) and the membrane water content Λ (i.e. $D_+(\Lambda) = \mathfrak{D}_+ \Lambda$), c_+ is the concentration of dissociated protons (full dissociation assumed), R is the gas constant and T the temperature.

3. 1. 2. Species Transport in Feed Parts

The transport of gaseous species in the feed parts addressed in the present paper differs from that in ref.²⁸ in that, that instead of a two-componential, it features a three-componential diffusion system on the cathode side. Thus a full derivation for a diffusion system of a ternary gas mixture is given.

Species transport in ideal gas is modelled by Stefan – Maxwell diffusion equations which, for the case of ternary gas mixtures (i.e. gas mixtures of three components as assumed in V) with the spectator species designated as solvent, read:⁴²

$$\mathbf{j}_g = \mathbf{u} c_g - D_{gg} \nabla c_g - D_{gr} \nabla c_r, \quad (3)$$

$$\mathbf{j}_r = \mathbf{u} c_r - D_{rr} \nabla c_r - D_{rg} \nabla c_g, \quad (4)$$

$$\mathbf{j}_s = \mathbf{u} (c_0 - c_g - c_r) + (D_{gg} + D_{rg}) \nabla c_g - (D_{rr} + D_{gr}) \nabla c_r, \quad (5)$$

where vectors \mathbf{j}_g , \mathbf{j}_r and \mathbf{j}_s are the molar fluxes of the three components: the gaseous water, the reactant (either oxygen for the cathode feed part or hydrogen for the anode feed part) and spectator species respectively, c_g , c_r and c_s are the corresponding molar concentrations, c_0 is the total molar concentration of the gas, \mathbf{u} is the net molar velocity

of the gas, $\nabla = (\partial_x, \partial_y, \partial_z)^T$ is the 3D nabla operator and D_{gg} , D_{gr} , D_{rg} , D_{rr} , are the ternary diffusion coefficients for the ternary solution of the three components which are functions of the corresponding binary coefficients and species concentrations.⁴²

$$D_{gg} = \frac{1}{\sigma} \left(\frac{c_g}{D_{gr}} + \frac{c_r + c_s}{D_{rs}} \right) \quad D_{gr} = \frac{c_g}{\sigma} \left(\frac{1}{D_{gr}} - \frac{1}{D_{gs}} \right),$$

$$D_{rg} = \frac{c_r}{\sigma} \left(\frac{1}{D_{gr}} - \frac{1}{D_{rs}} \right), \quad D_{rr} = \frac{1}{\sigma} \left(\frac{c_r}{D_{gr}} + \frac{c_s + c_g}{D_{gs}} \right), \quad (6)$$

$$\sigma = \frac{c_g}{D_{gr} D_{gs}} + \frac{c_r}{D_{gr} D_{rs}} + \frac{c_s}{D_{rs} D_{gs}},$$

where \mathfrak{D}_{gr} , \mathfrak{D}_{rs} and \mathfrak{D}_{gs} are the corresponding binary diffusion coefficients. Due to assumptions II and IV the temperature and pressure are constant and thus the total

molar concentration $c_0 = c_g + c_r + c_s = \frac{p}{RT}$ is also

constant which means that c_s is complementary to the sum $c_g + c_r$ and finding the distribution of all concentrations can be obtained by solving only equations (3), (4) and equation:

$$c_s = c_0 - c_g - c_r. \quad (7)$$

The anode gas is, as assumed in V, a binary mixture (no spectator species). For the case of binary gas mixtures the Stefan – Maxwell diffusion equations simplify, reading:⁴²

$$\mathbf{j}_g = \mathbf{v} c_g - \mathcal{D}_{gr} \nabla c_g, \quad (8)$$

$$\mathbf{j}_r = \mathbf{v} c_r - \mathcal{D}_{gr} \nabla c_r = \mathbf{v} (c_0 - c_g) + \mathcal{D}_{gr} \nabla c_g, \quad (9)$$

Taking equation (7) into account and adding together equations (3), (4) and (5) the expression for net molar velocity is obtained:

$$\mathbf{u} = \frac{\mathbf{j}_g + \mathbf{j}_r + \mathbf{j}_s}{c_0}. \quad (10)$$

Velocity is defined by the pressure gradient and differs for the region of the porous GDL and the empty space channel region. In the GDL the net gas flow is modelled by Darcy's law:^{18,43}

$$\mathbf{u} = -K \nabla p, \quad (11)$$

where K is the permeability of the porous medium. Following assumption IX the velocity field in the empty space of channel region is governed by the divergence free Navier-Stokes equation:⁴⁴

$$\mathbb{P}_{NS}\mathbf{u} = -\mu\nabla^2\mathbf{u} + \nabla \cdot (\mathbf{u} \otimes \mathbf{u}) = -\nabla p, \quad (12)$$

where \mathbb{P}_{NS} is the divergence free Navier-Stokes operator and μ is the dynamic viscosity of the gas.

At this point it is worth introducing a compact form of the diffusion equation. Gathering equations (3) and (4) yields an equation in terms of species vectors:

$$\begin{aligned} \begin{bmatrix} \mathbf{j}_g \\ \mathbf{j}_r \end{bmatrix} &= \begin{bmatrix} \mathbf{v} c_g \\ \mathbf{v} c_r \end{bmatrix} - \begin{bmatrix} D_{gg} & D_{gr} \\ D_{rg} & D_{rr} \end{bmatrix} \begin{bmatrix} \nabla c_g \\ \nabla c_r \end{bmatrix} = \\ &= \mathbf{v} \begin{bmatrix} c_g \\ c_r \end{bmatrix} - \begin{bmatrix} D_{gg} & D_{gr} \\ D_{rg} & D_{rr} \end{bmatrix} \nabla \begin{bmatrix} c_g \\ c_r \end{bmatrix}. \end{aligned} \quad (13)$$

By defining:

$$\begin{bmatrix} \mathbf{j}_g \\ \mathbf{j}_r \end{bmatrix} = \mathbf{J}, \quad \begin{bmatrix} c_g \\ c_r \end{bmatrix} = \mathbf{C}, \quad \begin{bmatrix} D_{gg} & D_{gr} \\ D_{rg} & D_{rr} \end{bmatrix} = \mathbf{D}, \quad (14)$$

the multi-component diffusion equation in compact form is given as:

$$\mathbf{J} = (\mathbf{v} - \mathbf{D} \nabla) \mathbf{C}. \quad (15)$$

Furthermore, the requirement for a steady state solution can be expressed as:

$$\frac{\partial \mathbf{C}}{\partial t} = -\nabla \cdot \mathbf{J} = \mathbf{D} \nabla^2 \mathbf{C} - \nabla \cdot (\mathbf{u} \mathbf{C}) = 0. \quad (16)$$

As far as mathematical formalism is concerned the difference between equations for binary diffusion systems (given in ref.²⁸) and ternary diffusion systems (presented here) is only in that equations for ternary mixtures deal with component doublets (\mathbf{J} and \mathbf{C} as defined in (14)) and a diffusion coefficient tensor instead of component singlets and a scalar binary diffusion coefficient that appear in equations for binary mixtures. The two-componential version of equation (16), applying to the anode binary gas mixture, thus reads:

$$\frac{\partial c_g}{\partial t} = -\nabla \cdot \mathbf{j}_g = \mathcal{D}_{gr} \nabla^2 c_g - \nabla \cdot (\mathbf{u} c_g) = 0, \quad (17)$$

where the reactant species is taken as the solvent component. The assumption of incompressible flow ($\nabla \cdot \mathbf{u} = 0$) requires that divergence of velocity be zero:

$$\text{div } \mathbf{u} = \nabla \cdot \mathbf{u} = \partial_x u_x + \partial_y u_y + \partial_z u_z = 0. \quad (18)$$

3. 1. 3. Coupling Species Transport Between Feed Parts and MEA

Equilibrium between the absorbed liquid water in the membrane and the gaseous water in the GDL is assumed at the MEA/GDL interface. Activity a of water vapour is simply its relative humidity:

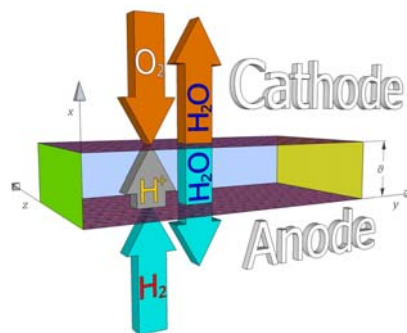


Figure 2.²⁸ Schematic representation of species production, consumption and transport in the MEA domain. The two ribbed purple surfaces represent the two catalyst layers at the two MEA/GDL interfaces. The brown arrows represent the species transport from/to cathode feed part, the cyan arrows the species transport from/to the anode feed part and the, the gray arrow represents the proton transport across the membrane. Hydrogen and oxygen are consumed at the anode and the cathode catalyst layers respectively. All the water is produced at the cathode catalyst layer and thus the molar flux of water traversing the membrane is equal to the flux entering the anode feed part.

$$a = \frac{c_g}{c_{sat}}, \quad (19)$$

where c_{sat} is concentration of saturated water vapor, while activity of absorbed water in membrane assumes relationship:⁹

$$\Lambda = \Lambda(a) = 0.043 + 17.8 a - 39.85 a^2 + 36 a^3. \quad (20)$$

On the two catalysts, which represent the interface between the MEA and the two feed parts, the rates of reactant consumption are defined:

$$\dot{n}_{O_2} = -\frac{i}{4F}, \quad (21)$$

$$\dot{n}_{H_2} = -\frac{i}{2F}, \quad (22)$$

where \dot{n}_{O_2} is the molar consumption per unit area of oxygen at the cathode catalyst layer and \dot{n}_{H_2} is the molar consumption of hydrogen at the anode catalyst layer. As discernible from Figure 2 the product water generated at the cathode catalyst surface diffuses into the cathode feed part and across the membrane into the anode feed part and, as indicated by the cyan “H₂O” arrow in Figure 2, the molar flux of water traversing the membrane is equal to the molar flux of water exiting the MEA and entering the anode feed part. Thus, summarising the MEA transport equations given in ref.²⁸ the two equations for the molar flux of water exchanged between the MEA the two feed parts read:

$$j_{AND} = -j_w = \frac{\mathcal{D}_w(\Lambda_{AND}^2 - \Lambda_{CTH}^2)}{2\vartheta} - n_{drg} \frac{i}{F} \quad (23)$$

where j_{AND} is the molar flux of water entering the anode feed part from the MEA and is, with respect to the orientation of the coordinate system in Figure 2, defined as positive when pointing in the negative x direction. And:

$$j_{CTH} = \left(\frac{1}{2} + n_{drg}\right) \frac{i}{F} - \frac{\mathcal{D}_w(\Lambda_{AND}^2 - \Lambda_{CTH}^2)}{2\vartheta} \quad (24)$$

where j_{CTH} is molar flux of water entering the cathode feed part from the MEA.

AND and *CTH* in superscript or subscript shall be generally used to denote values pertaining to the anode and the cathode side respectively.

3. 2. Electrochemical Reaction Kinetics

A fundamental quantity defining or influencing all species fluxes at the MEA/feed parts interfaces is the current density. Current density is given as a function of the cathode Galvani potential Φ (assumption XVI) by the Butler-Volmer equation:

$$i = B(\Phi, \zeta_r, \zeta_p) = i_{ex} \left(\frac{\zeta_r}{c_{ref}} e^{\frac{F\alpha}{RT}(\Phi^0 - \Phi)} - \left(\frac{\zeta_p}{c_{ref}} \right)^s e^{-\frac{F(1-\alpha)}{RT}(\Phi^0 - \Phi)} \right) \quad (25)$$

where $B(\Phi, \zeta_r, \zeta_p)$ denotes the Butler-Volmer function, i_{ex} is the surface exchange current density defined as current per unit area of catalyst layer, ζ_r and ζ_p are the reactant and product surface concentrations (in this case oxygen and water) respectively, c_{ref} is the reference concentration, s is the stoichiometry ratio, F is the faraday constant, α is the electron transfer coefficient and Φ^0 is the open circuit cathode Galvani potential at reference conditions (reference conditions mean that the species participating in the reduction reaction at the cathode assume reference concentration c_{ref}). The variable represented by $(\Phi^0 - \Phi)$ is not to be confused with the overvoltage.

4. HAN Approach to Solving Governing Equations

The modelled fuel cell is made of a number of equal parallel symmetrical ribs where a half of one such rib is indicated between the green and the yellow symmetry planes in Figure 1 (a). The symmetry between ribs allows no species flux across the symmetry plane (yellow surfaces in Figure 1). In the case of the two outermost ribs the fuel cell's wall boundary also allows no species flux across the wall. Taking into account also

that zero velocity in the direction of channel gas flow is assumed in GDL (assumption VIII), this wall boundary imposes same condition as the symmetry plane, which allows treating all ribs as identical. Since the two halves of one rib are mirror images and since all ribs are identical the fuel cell is a multiplication of one half of rib i.e. the so defined half of one rib is the representative unit of the fuel cell.

As depicted in Figure 1(b) and (c), the representative unit is sliced along the direction of the channel flow into a number of thin slices. Within each slice only the variation of variables in the plane perpendicular to the channel gas flow is addressed. This effectively makes a slice a 2D object. A slice has three parts: a cathode feed part, a membrane electrode assembly (MEA) part and an anode feed part. As discernible from Figure 1(d), the three parts are further divided onto seven computational domains: each feed part is divided into one channel domain and two GDL domains (GDL#1, GDL#2 as depicted in Figure 3) while the whole MEA part is contained within its MEA domain. The so defined computational domains, depicted in Figure 1 as shallow rectangular cuboids, share the 2D nature of a slice and are thus, in terms of mathematical modelling, simple rectangles.

The following sections 4.1 and 4.2 describe the HAN approach to solving the governing equations of transport, production and consumption of species in the individual domains. The complete analytic 2D solution for the distribution of species concentration in a slice is obtained by appropriately coupling the seven individual 2D solutions for each domain, i.e., the 2D solution for a slice is thus a jigsaw puzzle of the 2D solutions for each domain. This coupling is described in sections 3.1.3 and 4.3 that give the coupling conditions among domains of one slice. The 2D solutions of neighbour slices are coupled to one another via a 1D numerically resolved channel bulk flow yielding a solution for the whole representative unit, as described in section 4.5.

Obtaining 2D analytical solutions for slices and coupling them to one another via the perpendicular numerically resolved 1D gas flow gives this approach the name "hybrid 3D analytic-numerical". The HAN model thus gives full 3D information on species concentration distribution.

4. 1. Feed Part Domains

As presented in ref.²⁸ the hybrid 3D analytic numerical approach introduces a distinction that splits the general 3D notation into a 2D+1D notation reflecting the different treatment of physical phenomena in the dimensions perpendicular to the channel gas-flow and in the dimension along the channel gas-flow. The following equations of "2D+1D" type are derived for the ternary gas mixture and are analogous to those for binary mixtures given in ref.²⁸ with the difference that species component

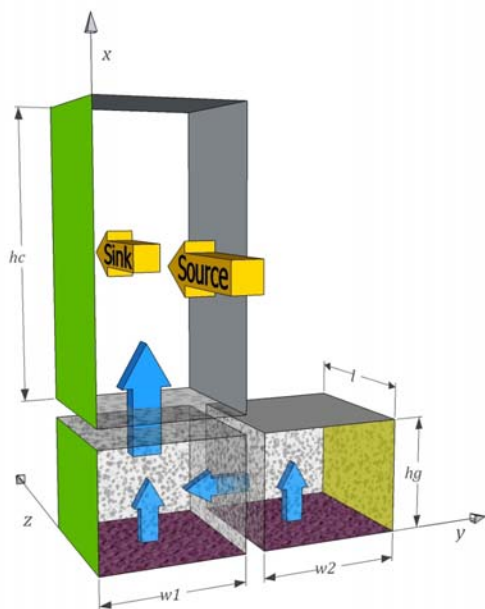


Figure 3.²⁸ Detailed schematic of feed part comprising three computational domains. The top cuboid is the channel domain, bottom left cuboid the GDL#1 domain and bottom right cuboid the GDL#2 domain. The “Source” arrow represents the convective species inflow from the channel domain of the previous upstream slice and the “Sink” arrow represents the species outflow into the channel domain of the next downstream slice. The blue arrows represent the molar fluxes of water traversing the borders between domains. These fluxes serve as boundary conditions for the individual solutions of domains. The ribbed purple surface represents the catalyst layer, i.e. the MEA/GDL interface. At the gray surfaces representing the walls, and at the green and yellow surfaces representing the two symmetry planes, the boundary condition requires zero flux across the boundary.

doublets and a diffusion coefficient tensor are used in place of component singlets and the scalar binary diffusion coefficient.

Placing the feed part into the coordinate system defined in Figure 3 the 2D nabla operator ∇ , the 2D Laplace operator ∇^2 , the 2D velocity β and the velocity component along the direction of channel gas flow v are defined in the cross-sectional plane as:

$$\nabla = \begin{pmatrix} \partial_x \\ \partial_y \end{pmatrix}, \quad \nabla^2 = \partial_x^2 + \partial_y^2, \quad \beta = \begin{pmatrix} u_x \\ u_y \end{pmatrix}, \quad v = u_z \quad (26)$$

(the 3D nabla ∇ should not be confused with its 2D version ∇). The condition in equation (18) can thus be rewritten as:

$$\partial_x u_x + \partial_y u_y + \partial_z u_z = 0 \Rightarrow \nabla \beta = -\partial_z v, \quad (27)$$

Rewriting equation (16) using the 2D+1D notation and neglecting the term $D(\partial^2 c)/(\partial z^2)$ (i.e. taking into account the assumption of no diffusive transport along the z coordinate VII) reads:

$$\begin{aligned} \frac{\partial C}{\partial t} &= D \nabla^2 C - \left(\nabla \cdot (\beta C) + \frac{\partial(v C)}{\partial z} \right) = \\ &= \frac{D \nabla^2 C - \nabla \cdot (\beta C)}{2D} - \frac{\partial(v C)}{1D} = 0. \end{aligned} \quad (28)$$

Equation (28) is solved for each feed part computational domain. Following the approximations and derivation in ref.²⁸ equation (28) is transformed into:

$$\frac{\partial C}{\partial t} = \frac{\nabla^2 (D C - \tilde{C} U)}{2D} - \frac{\partial_z (v C)}{1D} = 0, \quad (29)$$

where $\tilde{C} = \left[\bar{c}_r \right]$ is the average concentration in the relevant

computational domain (these average values of concentrations are also used to evaluate the tensor of diffusion constants D according to (6) and the 2D scalar field $U(x,y)$ is the velocity potential. Taking D and \tilde{C} as constants in the relevant channel domain makes equation (29) linear with respect to C and U . The approaches to solving equation (29) in the two types of feed part domains are the key of the HAN's modelling of species transport.

According to assumption VIII the velocity of gas in GDL has zero component along coordinate, i.e. $v = 0$. Thus, equation (29) in GDL is simplified to:

$$\frac{\partial C(x,y)}{\partial t} = \nabla^2 (D_{GDL} C(x,y) - \tilde{C} U(x,y)) = 0, \quad (30)$$

where D_{GDL} is the matrix of effective diffusion coefficients in GDL obtained according to assumption VI. Furthermore, the gas-flow in the GDL is governed by Darcy's law:

$$\beta = -\frac{k}{\mu} \nabla p = \nabla U, \quad (31)$$

where k is the GDL gas permeability and μ viscosity of the gas. The gas flow in the GDL is fully defined by the scalar field U or, in other words: gas-flow in the GDL is potential.

The governing equations for the gas flow in a channel are of the Navier-Stokes type generally meaning that the flow in channels is not potential. However, as shown in ref.²⁸ any non-potential part of the 2D velocity profile β vanishes in equation (29) and only the potential part comprehended in the velocity potential U is addressed.

Assumptions VII and VIII do not apply to the channel domain and thus the species transport along z coordinate does take place in channel domains and the term $\partial_z(v C)$ in equation (29) cannot be neglected since it plays an important role in the channel domain. The core of the HAN's numerical treatment of the gas flow in the channel, given in ref.²⁸ and extended to cover ternary mixtu-

res, is the finite-difference approximation for the derivative $\partial_z(vC)$:

$$\frac{\partial(vC)}{\partial z} \cong \frac{1}{l} \left((vC)|_{z=z_{exit}} - (vC)|_{z=z_{enter}} \right), \quad (32)$$

where $l = z_{exit} - z_{enter}$ is the depth of the slice with z_{enter} and z_{exit} denoting the values of z coordinate at the points where species flow enters and exits the channel domain respectively as indicated in Figure 3. Using approximation (32) in equation (29) yields:

$$\frac{\partial C_c}{\partial t} = \underbrace{\nabla^2(DC - \tilde{C}U)}_{2D} - \underbrace{\frac{1}{l} \left((vC)|_{z=z_{exit}} - (vC)|_{z=z_{enter}} \right)}_{1D} = 0. \quad (33)$$

Equation (33) can be interpreted as a simple species transport equation on a 2D plane with a source and a sink term: the *source* term being $\frac{1}{l}(vC)|_{z=z_{enter}}$ (i.e. the species inflow contribution) and the *sink* term being $-\frac{1}{l}(vC)|_{z=z_{exit}}$ (i.e. the species outflow contribution). This interpretation enables the species transport along the z coordinate and in the xy plane to be, within a channel domain, treated with a single 2D differential equation:

$$\frac{\partial C(x,y)}{\partial t} = \nabla^2(DC(x,y) - \tilde{C}U(x,y)) + S^{src}(x,y) - S^{snk}(x,y) = 0. \quad (34)$$

The source term S^{src} and the sink term S^{snk} , schematically represented by the two yellow arrows in Figure 3, are expressed as:

$$S^{src}(x,y) = \frac{1}{l} v^{pr}(x,y) C^{pr}(x,y), \quad (35)$$

$$S^{snk}(x,y) = \frac{1}{l} v(x,y) C(x,y), \quad (36)$$

where $v(x,y)$ is the cross-sectional profile of the z -component of the channel gas velocity and superscript *pr* denotes the values from the previous channel domain i.e. the channel domain in the upstream neighbour slice. According to assumption IX the velocity profile has always the same dome-like shape of laminar flow (as observed in Figure 4) scaled by the average velocity component in the channel domain in question:

$$v(x,y) = \bar{v} Y(x,y), \quad (37)$$

where \bar{v} is the average velocity component and $Y(x,y)$ is the unit-less dome shape as given in ref.²⁸. The variation of the average velocity component is calculated in a manner of a numerical 1D pipe flow model (given in section 4.4), i.e.: it

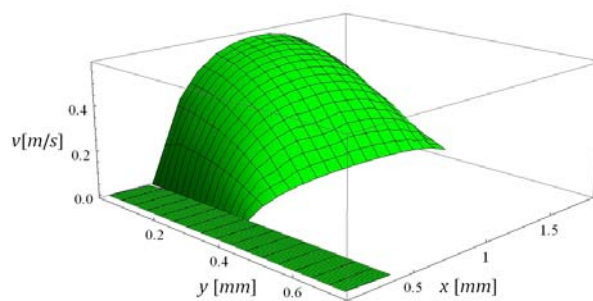


Figure 4.²⁸ Cross-sectional profile of z -component velocity of cathode gas at cross-section midway between inlet and outlet as obtained by CFD simulation. It is discernible from the plot that the z -component velocity in GDL ($0 < x < 0.285$ mm) is negligible and that the velocity profile in the channel assumes the dome shape of laminar flow.

is calculated stepwise from slice to slice according to the 1D gas-flow equation (43). The net convective flux into and out of the 2D of a slice plane (i.e. the sink and source terms) is thus obtained by multiplying the 2D velocity profile by the 2D species concentration distribution profile.

The 2D analytic general solution of the species concentration distribution and the velocity potential distribution U is obtained for every feed part domain as a linear combination of eigen functions of the ∇^2 operator (also called harmonics) with the geometry of that domain being their definition region. Since the definition regions of all computational domains are simple rectangles the eigen functions devised for each domain are the simple $\cos(k_x x)$, $\cos(k_y y)$ and $\cosh(k_x x) \cos(k_y y)$ functions. The full derivation of the eigen functions and the expression for the general solutions in domains as linear combinations of eigen functions is given in ref.²⁸.

4. 2. MEA Part

Unlike the feed parts that are each split onto three computational domains the whole MEA part is contained within its own computational domain as discernible from Figure 1 and Figure 2. The membrane species flux and concentration distribution is fully defined by the quantities j_{AND} , Λ_{AND} , j_{CTH} and Λ_{CTH} , which are defined on the MEA/anode and MEA/cathode interfacial surfaces. These quantities are thus within a slice one dimensional functions, i.e. $j_{AND} = j_{AND}(y)$, $\Lambda_{AND} = \Lambda_{AND}(y)$, $j_{CTH} = j_{CTH}(y)$ and $\Lambda_{CTH} = \Lambda_{CTH}(y)$. Also current density, cathode potential and reactant surface concentration are defined on the cathode catalyst surface which coincides with the MEA/cathode interface and thus these are also functions of y i.e.: $i(y)$, $\Phi(y)$, $\zeta_c(y)$. In order to couple appropriately to the general solutions of species concentration in the feed part domains, which come in the form of linear combinations of 2D $\cos(k_x x) \cos(k_y y)$ harmonics, HAN treats these surface quantities similarly in form of linear combinations of 1D $\cos(k_y y)$ harmonics.

4. 3. Boundary and Coupling Conditions at Domain Edges

Coupling of two general solutions in two domains that share an edge is done by fulfilling the conditions of continuity of species activity, of species molar fluxes, of net molar gas flows and of pressure at that boundary that is shared by the two domains. In addition to the expressions given in 3.1.3 that couple the MEA domain to the adjacent GDL domains the following summarises the couplings between pairs of feed part domains: Let subscripts $d1$ and $d2$ denote quantities pertaining to two domains sharing an edge, then the continuity conditions are expressed as follows:

species activity:

$$a_{d1}(\perp = edge) = a_{d2}(\perp = edge), \quad (38)$$

species molar fluxes:

$$\begin{aligned} \kappa_{d1} \frac{\partial (D_{d1} C_{d1}(x, y) - \tilde{C}_{d1} U_{d1}(x, y))}{\partial \perp} \Big|_{\perp = edge} \\ = \kappa_{d2} \frac{\partial (D_{d2} C_{d2}(x, y) - \tilde{C}_{d2} U_{d2}(x, y))}{\partial \perp} \Big|_{\perp = edge}, \end{aligned} \quad (39)$$

net molar gas flow:

$$\kappa_{d1} \frac{\partial U_{d1}(x, y)}{\partial \perp} \Big|_{\perp = edge} = \kappa_{d2} \frac{\partial U_{d2}(x, y)}{\partial \perp} \Big|_{\perp = edge}, \quad (40)$$

pressure (velocity potential):

$$U_{d1}(\perp = edge) = U_{d2}(\perp = edge), \quad (41)$$

where \perp denotes the coordinate that is perpendicular to the edge (x if edge runs along y and vice versa) and “edge” denotes the value of that coordinate at that edge. In the case of wall boundaries the boundary conditions read:

$$\frac{\partial U(x, y)}{\partial \perp} \Big|_{\perp = edge} = \frac{\partial C(x, y)}{\partial \perp} \Big|_{\perp = edge} = 0, \quad (42)$$

The specific boundary conditions are summarised in Table 1 where the following subscript notation is used in order to distinguish quantities in different feed part domains as defined in Figure 3: subscript c (as in e.g. C_c , β_c , U_c ...) pertains to the channel domain, subscript 1 pertains to the GDL#1 domain and subscript 2 to the GDL#2 domain.

4. 4. 1D Gas-flow Equations

The mean value of the z - component of the channel

domain gas velocity \tilde{v} , needed in equations (36) is given as:

$$\tilde{v} = \tilde{v}^{pr} + \frac{\dot{V}}{A} \quad (43)$$

where \tilde{v}^{pr} is the z -component of the gas velocity in the previous upstream channel domain, $A = w1 \times h2$, as discernible from Figure 3, is the channel cross-sectional area and \dot{V} is the net gas volume flux exchanged between the GDL#1 and the channel domain within the slice depth defined as:

$$\dot{V} = l \int_0^{w1} \beta_{1 \rightarrow c}(y) dy \quad (44)$$

where l is the slice depth and $\beta_{1 \rightarrow c}(y)$ is the gas velocity component perpendicular to the boundary between the GDL#1 and the channel domain evaluated at that boundary.

4. 5. Solution for the Whole Representative Unit

The core principle of HAN modelling approach is obtaining a general analytic solution of the 2D diffusion problem in each of the seven computational domain types (Figure 1 (d)). This is done by finding the domain specific eigen functions (also called harmonics) of the ∇^2 operator. These harmonics are 2D trigonometric functions characterised by mode numbers and m with n numbering modes along x coordinate and m modes along y coordinate. (A full detailed construction of these eigen functions is given in ref:²⁸). For each domain the specific solution comes in the form of a specific linear combination of its eigen functions, i.e. a 2D type Fourier series. Finding the specific solution for the species concentration and the velocity potential in the whole representative unit thus means finding all Fourier coefficients in the linear combinations of eigen functions of the seven computational domains in every slice. These Fourier coefficients are defined when coupling domains to one another, which is explained in detail in ref:²⁸.

In the co-flow configuration featured in ref:²⁸ there is a single channel flow direction, slices can be uniquely ordered and consecutive solutions for individual slices can be sought. However, in the counter-flow regime there are two opposite directions of channel flow and the anode feed part, the cathode feed part and the MEA part have to be addressed separately.

In the counter-flow configuration two independent series of consecutive specific solutions are sought: one for only the cathode feed part of slices and one for only the anode feed part of slices. These two specific solutions for the two whole feed parts are obtained by decoupling the two feed parts from the MEA part and assuming the spe-

Table 1. Summary of key governing equations and their boundary conditions.

GDL domains	
	Governing equation $\nabla^2 (D_{GDL} C_1(x, y) - \tilde{C}_1 U(x, y)) = 0$
Species transport	Boundary conditions $\frac{\partial C_2(x, y)}{\partial x} \Big _{x=h_1} = \frac{\partial C_2(x, y)}{\partial y} \Big _{y=w} = \frac{\partial C_1(x, y)}{\partial y} \Big _{y=0} = 0,$ $\frac{\partial (D_{GDL} C_1(x, y) - \tilde{C}_1 U_1(x, y))}{\partial y} \Big _{y=w_1} = \frac{\partial (D_{GDL} C_2(x, y) - \tilde{C}_2 U_2(x, y))}{\partial x} \Big _{y=w_1},$ $\kappa \frac{\partial (D_{GDL} C_1(x, y) - \tilde{C}_1 U_1(x, y))}{\partial x} \Big _{x=0} = j_{M-1}(y),$ $\kappa \frac{\partial (D_{GDL} C_2(x, y) - \tilde{C}_2 U_2(x, y))}{\partial x} \Big _{x=0} = j_{M-2}(y),$ $\kappa \frac{\partial (D_{GDL} C_1(x, y) - \tilde{C}_1 U_1(x, y))}{\partial x} \Big _{x=h_1} = j_{1-c}(y)$
	Governing equation $\nabla^2 U(x, y) = 0$
	Boundary conditions $\frac{\partial U_2(x, y)}{\partial x} \Big _{x=h_1} = \frac{\partial U_2(x, y)}{\partial y} \Big _{y=w} = \frac{\partial U_1(x, y)}{\partial y} \Big _{y=0} = 0,$ $c_0 \kappa \frac{\partial U_1(x, y)}{\partial x} \Big _{x=0} = j_{M-1}(y) - j_{r1}(y),$ $c_0 \kappa \frac{\partial U_2(x, y)}{\partial x} \Big _{x=0} = j_{M-2}(y) - j_{r2}(y),$ $\frac{\partial U_1(x, y)}{\partial y} \Big _{y=w_1} = \frac{\partial U_2(x, y)}{\partial x} \Big _{y=w_1},$ $U_1(x = h_1, y) = -\frac{k}{\mu} p_c$
Channel domain	
	Governing equation $\nabla^2 (D C_c(x, y) - \tilde{C}_c U(x, y)) + S^{src}(x, y) - S^{snk}(x, y) = 0$
Species transport	Boundary conditions $S^{src}(x, y) = \frac{1}{l} v^{pr}(x, y) C_c^{pr}(x, y),$ $S^{snk}(x, y) = \frac{1}{l} v(x, y) C_c(x, y),$ $\frac{\partial C_c(x, y)}{\partial x} \Big _{x=h} = \frac{\partial C_c(x, y)}{\partial y} \Big _{y=w_1} = \frac{\partial C_c(x, y)}{\partial y} \Big _{y=0} = 0,$ $D \frac{\partial (D C_c(x, y) - \tilde{C}_c U_c(x, y))}{\partial x} \Big _{x=h_1} = j_{1-c}(y),$
	Governing equation $\nabla^2 U(x, y) = \frac{(v(x, y, z = z_{enter}) - v(x, y, z = z_{exit}))}{l}$
Velocity profile	Boundary conditions $\frac{\partial U_c(x, y)}{\partial x} \Big _{x=h} = \frac{\partial U_c(x, y)}{\partial y} \Big _{y=w_1} = \frac{\partial U_c(x, y)}{\partial y} \Big _{y=0} = 0,$ $\frac{\partial U_c(x, y)}{\partial x} \Big _{x=h_1} = \beta_{1-c}(y)$
MEA domain	
	Governing equation $j_w = d_w \frac{(\Lambda_{AND}^2 - \Lambda_{CTH}^2)}{g} - n_{drg} \frac{i}{F}$
Species transport	Boundary conditions $\Lambda_{AND}(y) = \begin{cases} \Lambda(a_1^{AND}(x = 0, y)), & 0 \leq y < w_{1AND} \\ \Lambda(a_2^{AND}(x = 0, y)), & w_{1AND} \leq y < w' \end{cases}$ $\Lambda_{CTH}(y) = \begin{cases} \Lambda(a_1^{CTH}(x = 0, y)), & 0 \leq y < w_{1CTH} \\ \Lambda(a_2^{CTH}(x = 0, y)), & w_{1CTH} \leq y < w \end{cases}$
Electrochemical kinetics	$i = (\Phi - V_{op}) \frac{F d_+ (\Lambda_{AND} + \Lambda_{CTH})}{2\theta} = i_{ex} \left(\frac{c_r}{c_{ref}} e^{\frac{F\alpha}{RT}(\Phi^0 - \Phi)} - \left(\frac{c_p}{c_{ref}} \right)^s e^{-\frac{F(1-\alpha)}{RT}(\Phi^0 - \Phi)} \right)$

cies fluxes across the two MEA/GDL interfaces as given parameters instead of being bound by the coupling condi-

tions. Within a feed part of a slice the assumed species flux across the corresponding MEA/GDL interface comes

in the form of a Fourier series and thus all Fourier coefficients in the linear combinations of eigen functions of the three computational domains in one feed part of a slice are fully defined by the corresponding source term and that parameter of species flux across the MEA/GDL interface. Given that these parameters for species flux across the MEA/GDL interfaces are available a 3D solution for one whole feed part is obtained as a series of consecutive 2D solutions for the slices of that feed part. As reasoned in the co-flow case in ref.²⁸, the governing equations of species transport in the domains of the feed parts are linear differential equations and thus this solution is obtained by linear algebra. A 3D solution for the whole MEA part is obtained in a similar manner, that is, by assuming the species concentration at the two MEA/GDL interfaces as given parameters (again in the form of Fourier series). Obtaining a solution for the MEA domains involves taking into account also the nonlinear electrochemical equations and in the nonlinear relationship of activity to water content dependence. These nonlinear phenomena are, as in the co-flow case in ref.²⁸, treated using the derivative approximation. In counter-flow configuration the estimation-iteration is performed on a different level than in co-flow configuration and is used for achieving the coupling between the MEA part and the two feed parts. The derivative approximation and the estimation-iteration routines are described in the following two paragraphs.

4. 5. 1. Derivative Approximation

The approach of derivative approximation and estimation-iteration is based on substituting the nonlinear functions such as $B(\Phi(y), \zeta_r(y), \zeta_p(y))$, $R(\Lambda_{AND}(y), \Lambda_{CTH}(y)) \dots$ with their linear approximations. This approach assumes that within a slice each argument of these nonlinear functions (i.e. $\Phi(y)$, $\Lambda_{AND}(y)$, $\zeta_r(y)$) ... features only small deviations from its average along the y coordinate. Let f_{NL} stand for any of the aforementioned nonlinear functions and let \arg_1, \arg_2, \dots stand for its arguments:

$$f_{NL}(y) = f_{NL}(\arg_1(y), \arg_2(y), \dots). \quad (45)$$

Each argument of the nonlinear function is split into two parts:

$$\arg(y) = \Pi + \Delta\arg(y), \quad (46)$$

where \arg stands for any of the arguments, Π is a predictor of the average value of \arg over y (not necessarily the average itself but a close estimate of it) and $\Delta\arg(y)$ is the deviation from the predictor Π along y . The assumption of small deviations means that $\Delta\arg(y)$ is always sufficiently small to justify the following derivative approximation:

$$\begin{aligned} f_{NL}(y) &\cong \\ f_{NL}(\Pi_1, \Pi_2, \dots) &+ \left. \frac{\partial f_{NL}}{\partial \arg_1} \right|_{\substack{\arg_1 = \Pi_1 \\ \arg_2 = \Pi_2 \\ \dots}} \Delta\arg_1(y) + \\ &+ \left. \frac{\partial f_{NL}}{\partial \arg_2} \right|_{\substack{\arg_1 = \Pi_1 \\ \arg_2 = \Pi_2 \\ \dots}} \Delta\arg_2(y) + \dots = \\ &= f_L(\Delta\arg_1(y), \Delta\arg_2(y), \dots) \end{aligned} \quad (47)$$

where f_L is a linear function of deviations $\Delta\arg_1(y)$, $\Delta\arg_2(y) \dots$ and due to the linear nature of equation (46) f_L is thus also a linear function of the arguments $\arg_1(y)$, $\arg_2(y), \dots$. The nonlinear function f_{NL} is therefore linearised by substituting it with its corresponding f_L (pink box in Figure 5). The specific linearization equations for the nonlinear functions used in the HAN model are given in ref.²⁸.

4. 5. 2. Estimation-Iteration

The counter-flow algorithm is explained using Figure 5 that shows the fuel cell split according to the two different types of calculation:

- Calculation of the feed part elements, i.e. the two rows of light brown (cathode) and light gray (anode) boxes in the top part of Figure 5 and
- calculation of the MEA part elements, i.e. the row of light blue boxes representing the MEA part in the bottom part of Figure 5.

Let Π^J be the predictor for all Fourier coefficients for all Fourier series of the species flux across MEA/GDL interfaces in all slices and let Π^C be the predictor for all Fourier coefficients for all Fourier series of the species concentrations at MEA/GDL interfaces in all slices. Π^C and Π^J are used as the two parameters at the MEA/GDL interfaces defined above. The estimation iteration routine starts with some first estimate for Π^C . Using this Π^C predictor estimate as the parameter defining the species concentrations at the MEA/GDL interfaces the individual 2D solutions for the MEA part slices are obtained by first linearizing the nonlinear functions with the derivative approximation defined in equation (47) (pink box in Figure 5) and then using the linearized functions for solving the 2D MEA linear algebraic equations (given in ref.²⁸) (bottom blue box in Figure 5). The so obtained series of 2D solutions gives full information on concentration and velocity potential distribution and thus gives also the values of $j_{AND}(y)$, $j_{CTH}(y)$, $\dot{n}_{O_2}(y), \dots$, i.e. the species flux across the MEA/GDL interfaces. Let \mathbf{J} denote all Fourier coefficients for all Fourier series of the so obtained species concentrations at MEA/GDL interfaces in all slices. Setting the value of the Π^J predictor to the value of the newly obtained \mathbf{J} :

$$\Pi^J = \mathbf{J}, \quad (48)$$

and using Π^j as the parameter defining the species fluxes across the MEA/GDL interfaces the individual 2D solutions for the 3D solution for the anode and the cathode feed part are calculated using the 2D linear algebra (upper blue box in Figure 5). The so obtained algebraic solutions give, among others, also the values of the species concentrations at the MEA/GDL interfaces. Let C denote all Fourier coefficients for all Fourier series of the so obtained species concentrations at MEA/GDL interfaces in all slices. The value of C is compared to the current value of the

Π^C predictor (yellow box in Figure 5) and if the difference between the two is above the convergence criteria (red box in Figure 5) the Π^C predictor value is set to the value of the newly obtained C :

$$\Pi^C = C. \quad (49)$$

The procedure is repeated with the new value Π^C predictor value and so on till a positive result (green box) of the convergence criteria test. Together with the repeated

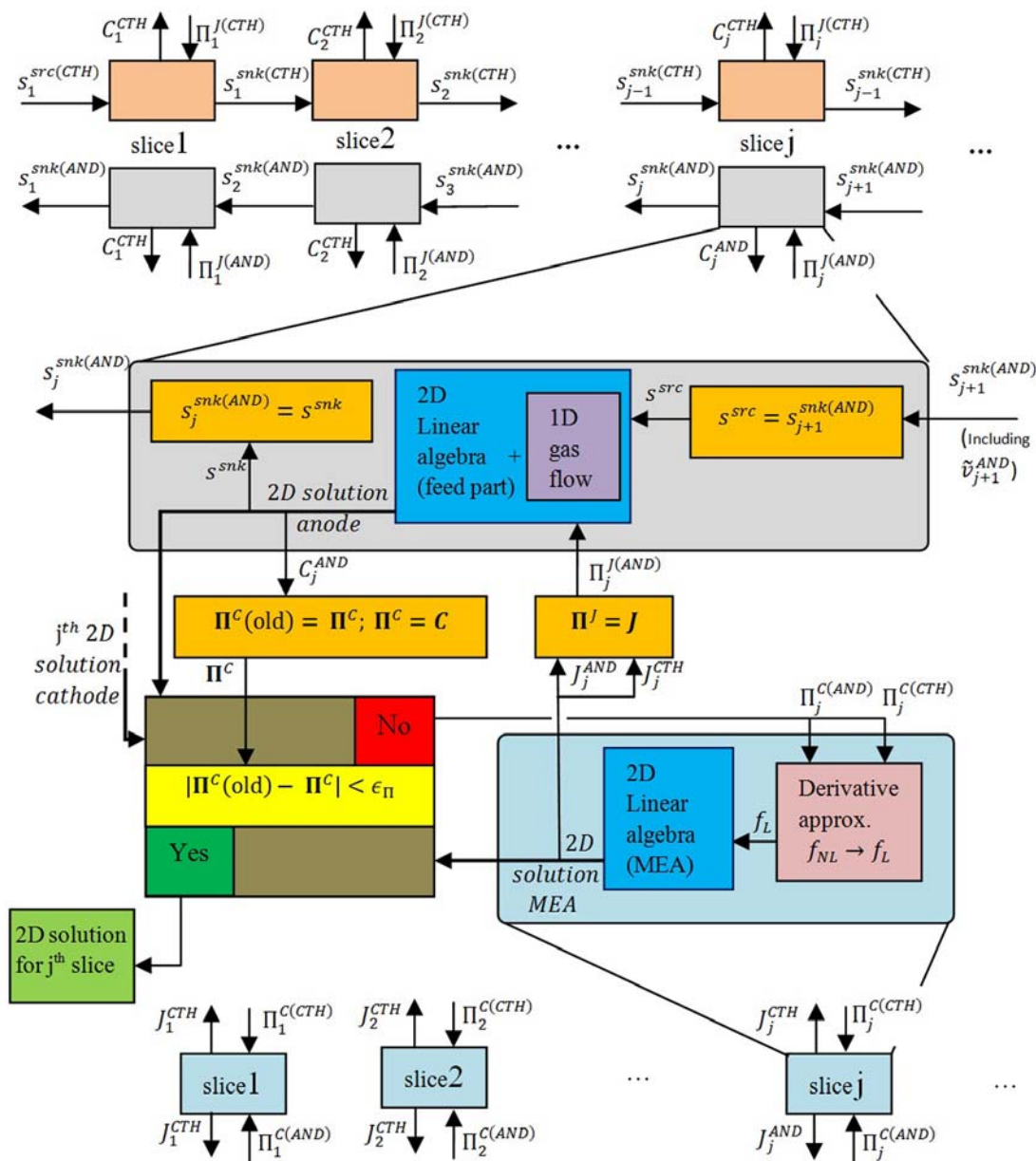


Figure 5. Counter-flow calculation procedure for obtaining the solution for the whole representative unit. The light brown, light grey and light blue boxes represent the cathode feed part, the anode feed part and the MEA domains respectively. Specific computational steps for cathode feed part domain are not shown since they are identical to those for anode feed part domain. The values of source/sink terms include also the information on the mean z-component velocity. Symbols in bold denote sets of all variables/parameters of the same type, i.e., e.g.:

$$C = \{C_1^{CTH}, C_1^{AND}, \dots, C_j^{CTH}, C_j^{AND}, \dots\}, \Pi^C = \{\Pi_1^{C(CTH)}, \Pi_1^{C(AND)}, \dots, \Pi_j^{C(CTH)}, \Pi_j^{C(AND)}, \dots\};$$

re-evaluation of C also the mean value of the z - component of the channel gas velocity \tilde{v} is repeatedly re-evaluated (purple box) in Figure 5.

Renewing the predictor values directly with the newly obtained values of J and C typically leads to numerical instabilities. Thus numerical relaxation is used and instead of equations (48) and (49) the predictors are renewed using relaxation:

$$\begin{aligned}\Pi^C(\text{new}) &= \omega_{rlx}^C \Pi^C(\text{old}) + (1 - \omega_{rlx}^C) C, \\ \Pi^J(\text{new}) &= \omega_{rlx}^J \Pi^J(\text{old}) + (1 - \omega_{rlx}^J) J.\end{aligned}\quad (50)$$

where (*new*) denotes the renewed value of predictor and (*old*) the previous value and ω_{rlx}^C and ω_{rlx}^J are the corresponding relaxation coefficients.

5. Simulation Setup

The HAN fuel cell modelling principles were applied to model a laboratory experimental fuel cell (schematically depicted in Figure 1) of which geometrical and material properties are summarised in Table 2.²⁸

Using the operational parameters summarised in Table 1 the operation at a number of different operational voltages was simulated.

The HAN results on polarisation characteristics were comparatively evaluated against CFD polarisation results. The CFD results were obtained by a validated CFD model.^{45,46} In addition to the comparison of the polarisation results the HAN's simulation results on spatial distribution of important physical quantities were also compared.

Table 2. Parameters defining operational conditions.

Parameter	Symbol	Value
Operational voltages	V_{op}	0.855, 0.813, 0.787, 0.751, 0.721, 6.9, 6.56V
Pressure*	p	$1.0 \cdot 10^5 \text{ Pa}$
Temperature	T	343.15 K
Inlet gas velocity (anode and cathode)	–	0.4 m/s
Inlet gas relative humidity (anode & cathode)	$\frac{c}{c_{sat}}$	0.5

* In CFD this is the value of outlet pressure, maximal deviations from this value anywhere in the representative unit are +0.53% and –0.28% justifying assumption IV of isobaric HAN.

Table 2. Geometrical and material parameters used in HAN and CFD models.

parameter	Symbol	Value
Channel height (anode and cathode)	h_2	$1.5 \cdot 10^{-3} \text{ m}$
Membrane thickness	ϑ	$3.5 \cdot 10^{-3} \text{ m}$
Half of anode channel width	w_{1AND}	$2.5 \cdot 10^{-4} \text{ m}$
Half of cathode channel width	w_{1CTH}	$3.75 \cdot 10^{-4} \text{ m}$
GDL thickness (anode and cathode)	h_1	$2.85 \cdot 10^{-4} \text{ m}$
width of representative unit	w	$7.5 \cdot 10^{-4} \text{ m}$
length of Representative unit	L	$2.7 \cdot 10^{-2} \text{ m}$
GDL void space volume fraction (anode and cathode)	κ	0.78
	$\frac{D}{D_{GDL}}$	1.34
GDL tortuosity (anode and cathode)	c_{HSO_3}	1900 mol/m^3
Membrane sulphonic group concentration	α	0.855
Cathode charge transfer coefficient	c_{sat}	$3.12 \cdot 10^4 \text{ Pa}$
saturated water vapour partial pressure at 343.15K	\mathcal{D}_{rg}	$3.98 \cdot 10^{-5} \text{ m}^2/\text{s}$
$\text{H}_2\text{O}_{(g)}/\text{O}_2$ binary diffusion coeff. (at 343.15K)*	\mathcal{D}_{rg}	$1.12 \cdot 10^{-4} \text{ m}^2/\text{s}$
$\text{H}_2\text{O}_{(g)}/\text{H}_2$ binary diffusion coeff. (at 343.15K) ¹	\mathcal{D}_{gs}	$4.16 \cdot 10^{-5} \text{ m}^2/\text{s}$
$\text{H}_2\text{O}_{(g)}/\text{N}_2$ binary diffusion coeff. (at 343.15K) ¹	\mathcal{D}_{rs}	$2.95 \cdot 10^{-5} \text{ m}^2/\text{s}$
N_2/O_2 binary diffusion coeff. (at 343.15K) ¹	\mathcal{D}_w	$2.1 \cdot 10^{-7} \text{ m}^2/\text{s}$
Coefficient of proportionality to water content of water diffusion coefficient in membrane (at 343.15K)	\mathcal{D}_+	$1.6 \times 10^{-8} \text{ m}^2/\text{s}$
Coefficient of proportionality to water content of proton diffusion coefficient in membrane (at 343.15K)	–	$1.125 \times 10^{-3} \text{ m}$
Cathode reaction layer thickness (CFD only)	–	$4.7 \times 10^3 \text{ A/m}^2$
Cathode exchange current density (CFD only)**	i_{ex}^*	0.1195 A/m^2
Effective cathode surface exchange current density (HAN only)		

* In CFD these are the mean values since the CFD simulation takes into account the dependence of binary diffusion coefficient on the ratio of the components. However, the relative standard deviation is below 0.09% with maximal deviations from the mean value anywhere in the representative unit being +0.45% and –0.26% justifying the assumption V, i.e. the use of component ratio independent binary diffusion coefficient in HAN.

** The user manual of the CFD software gives insufficient information on what temperature or other conditions this exchange current density parameter pertains to. This is thus only raw model input data.

ratively evaluated against the corresponding CFD results. The results are given in section 6. To make the simulation results of HAN and CFD models as comparable as possible all material and operational parameters that apply to both HAN and CFD were set to the same values in the settings of both models. Table 2 summarizes the parameters used in the CFD and the HAN models. The parameters marked with “(HAN only)” and “(CFD only)” pertain only to the CFD and HAN respectively, whereas all others pertain to both. Reflecting the assumption of infinite thinness of the catalyst layer (XVII) made by the HAN approach an effective cathode surface exchange current density is defined for the HAN model. The value for this effective cathode surface exchange current density is taken from ref.²⁸.

CFD simulation was done using AVL FIRE® v2011 with the “Fuel cell” module (validation of which is found in refs.^{45,46}). Two meshes differing in meshing density were used for simulations. The denser mesh was used for obtaining results with high spatial resolution needed for plotting smooth 3D graphs in the results section. The coarser mesh was used for estimating the shortest computational times of a CFD simulation that still gives accurate results on current density. The two meshes were identical as those used in ref.²⁸, where the meshing details are given.

HAN model was programmed in Wolfram Mathematica 9.0.1. In HAN the representative unit was sliced into 20 sections (slices) along the direction of gas flow and the first 3 modes per each coordinate. (i.e. 3 modes along y and 3 modes along x coordinate) were taken into account in harmonics in each gas part computational domain.

6. Results

The calibrated value of the effective exchange current density reported in ref.²⁸ was used in the HAN model presented in this paper. The HAN model is evaluated globally by a comparative plot of the polarisation curve and locally by a detailed comparative analysis of spatial distribution of key variables at the operating point of highest current density.

To aid the interpretation of the graphs in the following figures Figure 6 shows the modelled representative unit placed in the coordinate system with respect to which all graphs of CFD and HAN-FC results are plotted. It should be noted that the choice of directions and origins of coordinates in Figure 6 is such that it enables easy interpretation of the graphs in this section and differs from the choice in Figure 2 or Figure 3 where the coordinate directions and origins are chosen in such a way to best suit expressions of governing equations in section 3. Additionally it should be noted that the gap between anode and cathode GDL in Figure 6 does not reflect the thickness of the membrane.

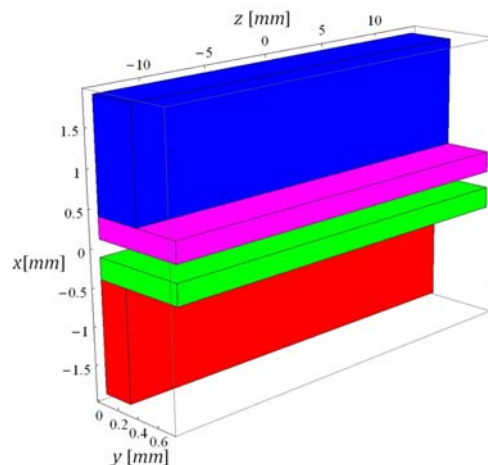


Figure 6.²⁸ Representative unit in coordinate system. Cathode channel is coloured blue, cathode GDL magenta, anode GDL green and anode channel red. The central symmetry plane of a rib and the symmetry plane between ribs (respectively depicted as green and yellowish surfaces in Figure 1) that define representative unit are at $y = 0$ and at $y = 0.75 \text{ mm}$ respectively. The anode inlet and the cathode outlet are at $z = -13.5 \text{ mm}$ and the cross-sectional plane midway between inlet and outlet is at $z = 0$.

6. 1. Plots of Comparative Results

In this subsection a number of comparative results are presented where in all graphs the CFD results are coloured green and are obtained using the denser mesh and HAN results are coloured brown.

Figure 7 shows the polarisation curve as calculated by the CFD and by the HAN where the points are obtained by calculating current density at five predefined operational voltages (with all other operational parameters fixed) as reported in Table 1.

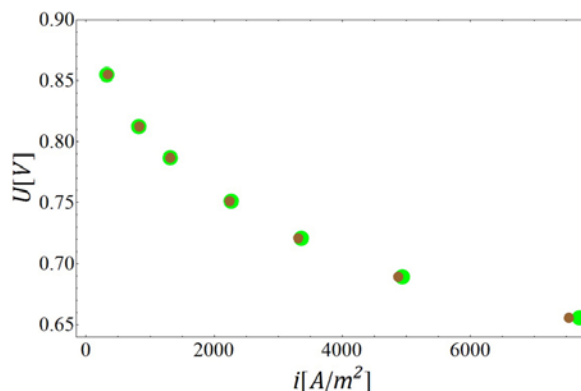


Figure 7. Polarisation curve of current density obtained at seven different voltages (Table 3). Brown are HAN and green CFD results.

The most important simulation result is the current density distribution, which is plotted in Figure 8. The close agreement between HAN and CFD results in Figure 7

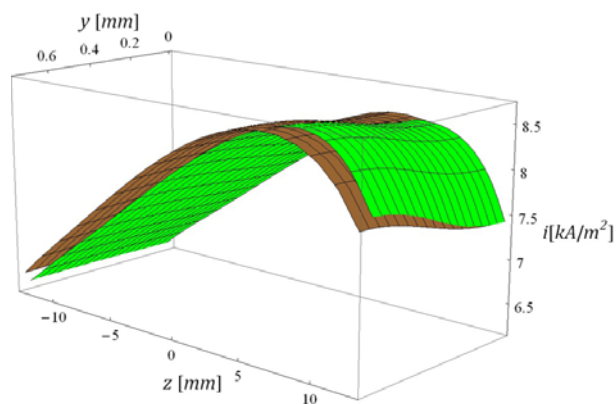


Figure 8. 3D plot of current density distribution over whole catalyst surface of the representative unit at 0.656V. Green are CFD results and brown HAN-FC results.

and Figure 8 speaks of high level of fidelity of the HAN model. However the difference between the results obtained by HAN and by CFD in this figure is larger than the one observed in the co-flow case in ref.²⁸. Therefore it is instructive to analyse the underlying physical phenomena responsible for the trends seen in Figure 8.

There are two major factors influencing the local values of current density: the oxygen concentration at the cathode catalyst surface, plotted in Figure 9, and the membrane proton conductance, which is, according to equation (2), linearly proportional to the mean membrane water content plotted in Figure 10. Oxygen is consumed on the way from the cathode inlet to the cathode outlet and the graph of oxygen concentration at catalyst surface shows the expected decreasing trend in this direction. Also notable is the decrease in the oxygen surface concentration at higher values of y , which is the consequence of the regions at higher values of y being farther from the channel that supplies the oxygen. The oxygen surface concentration plots in Figure 9 show a very close agreement between HAN and CFD and thus cannot explain the difference in the two plots of current density in Figure 8. A bigger difference between HAN and CFD plots is observable in the plots of mean membrane water content. Again, as explained in ref.²⁸, the higher values of membrane water content at higher values of y is due to a higher water vapour build-up in the GDL#2 domains compared to GDL#1 domains which leads to more hydrated and thus more conductive regions of membrane that are adjacent to the GDL#2 domains. The mean membrane water content is the lowest at both inlet/outlet ends of the representative unit due to the relatively dry (50% relative humidity) reactant gasses fed at both inlets as discernible in Figure 11. The lower membrane water content at the cathode outlet/anode inlet is explained with the poorer hydration due to the lower current density (lower rate of water production) at that end compared to the cathode inlet/anode outlet end. This difference in

current density at the two ends is explained by the fact that the oxygen concentration is lower at the cathode outlet. The difference in the HAN and CFD plots of the mean membrane water content is the result of differences in the membrane model (e.g. HAN neglects proton back diffusion) and the nonlinearity of the function of membrane water content to activity dependence (20), which translates small differences in water activity into relatively larger differences in membrane water content. However the differences between HAN and CFD simulated membrane water content do not linearly translate into differences between the simulated current density since a positive difference in current density leads to a negative difference in cathode potential (plotted in Figure 12), which leads to a negative difference in membrane voltage drop resulting in smaller relative differences in current densities between CFD and HAN (Figure 8) compared to the relative differences in membrane hydration in Figure 10.

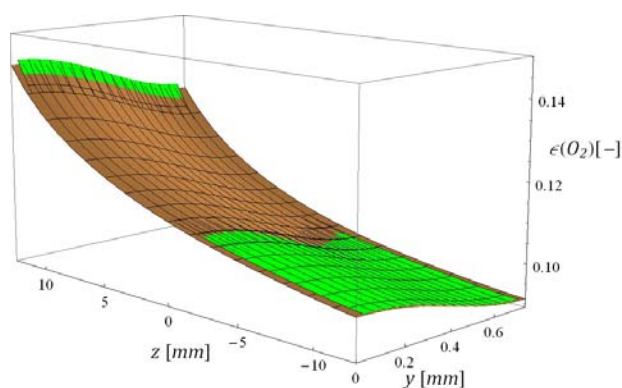


Figure 9. Cathode catalyst surface mole fraction of oxygen $\epsilon(O_2)$ at 0.656V of operational voltage. Green plot are CFD results and brown HAN results.

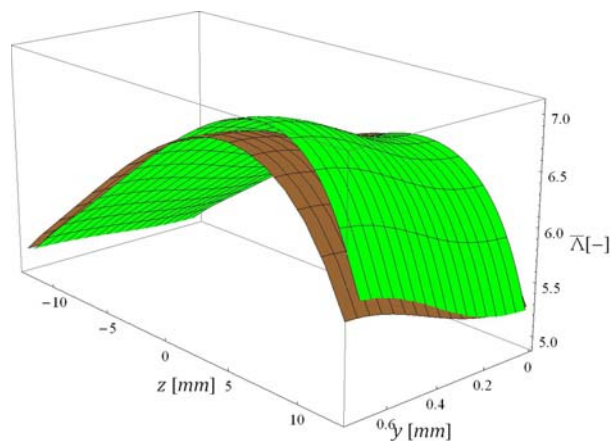


Figure 10. Mean membrane water content at 0.656V of operational voltage. Green plot are CFD results and brown HAN results.

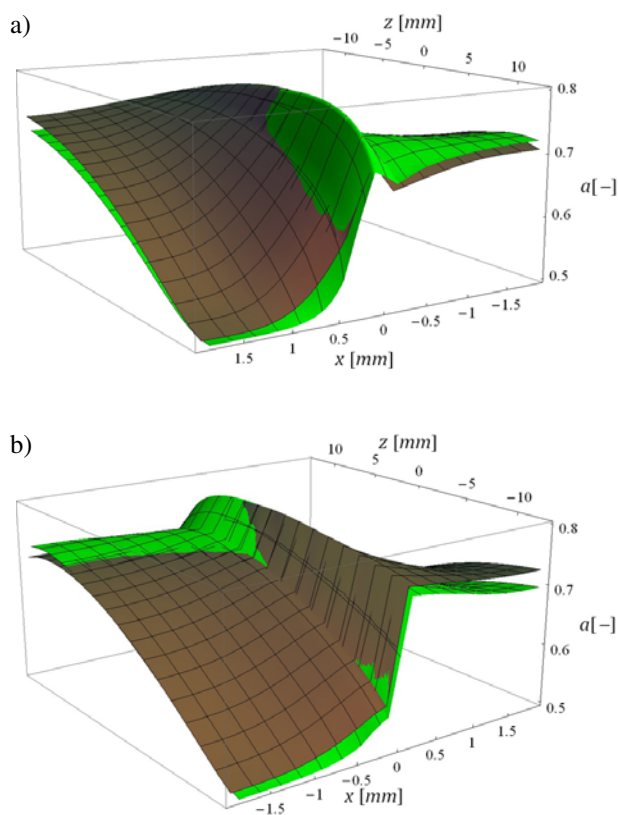


Figure 11. Water activity (relative humidity) on the central symmetry plane of a rib at 0.656V. **a)** view with cathode inlet/anode outlet in front; **b)** view with anode inlet/cathode outlet in front. Values in the membrane are obtained by interpolating values at the anode and cathode GDL /MEA interfaces.

It is also valuable to compare HAN to CFD with the results on species concentration distribution presented in Figure 11 and Figure 13. The brown plot in Figure 13 represents HAN's full 2D analytic solution for water vapour concentration distribution in the slice at the cathode inlet/anode outlet. The comparative graphs in Figure 13 and Figure 11 show that the largest difference between HAN and CFD appears at both outlets. This is the consequence of the small differences in current density and resulting species fluxes accumulating along the gas path.

Overall Figure 7 to Figure 13 show a very good agreement between CFD and HAN-FC in terms of trends

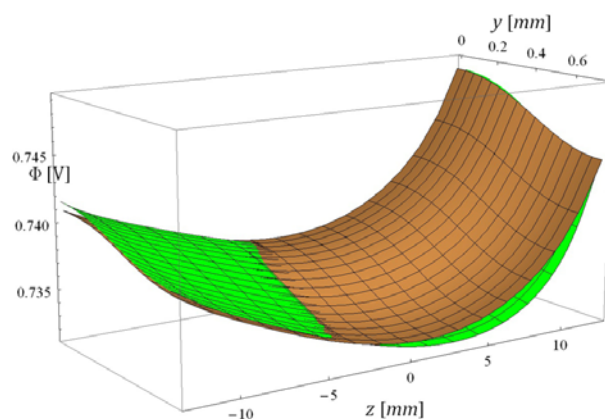


Figure 12. Cathode Galvani potential distribution at 0.656V of operational voltage. Green plot are CFD results and brown HAN results.

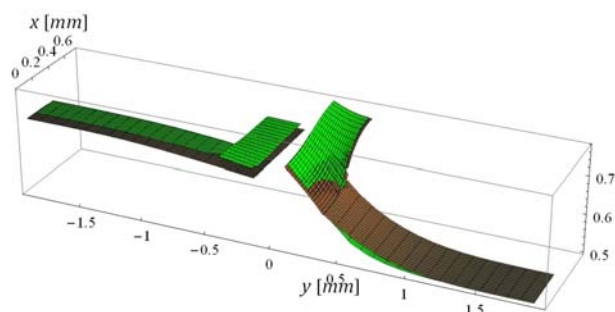


Figure 13. Relative humidity in the slice at the cathode inlet/anode outlet i.e. $z = 13.5 \text{ mm}$ at 0.656V. Green plot are CFD results and brown HAN results.

in analysed variables and in terms of their absolute values confirming the capability of HAN to model species transport in ternary gas mixtures and validating the computational algorithm for the counter-flow configuration.

6. 2. Computational Times

Table 3 shows computational times for the HAN model and the CFD model with two different mesh resolutions (i.e. number of volume elements).

Table 3. Calculation times (on a desktop computer)

Model	Resolution	No. of iterations	CPU cores used	CPU time [s]	Total time [s]
CFD(denser)	34560 vol. el.	50 000	4	38 000	13 000
CFD(coarser)	4320 vol. el.	20 000	4	2400	640
HAN	3 modes	60	1	20*	20*

* Times obtained with HAN programmed in Mathematica – considerably shorter times are expected for HAN programmed in C or Fortran.

The denser CFD mesh features twice as many divisions along each coordinate as coarser one amounting to 8 times more volume elements. Larger number of volume elements also requires more iterations to reach adequate convergence. The large difference between computational times of HAN and those of CFD originates from the fact that CFD requires few thousand iterations of the solution for the whole mesh to reach convergent results, whereas the HAN's algorithm for counter-flow regime requires only 50 to 100 iterations. However this is still considerably more than the equivalent 5 to 6 iterations needed for each slice in the co-flow regime as reported in ref.²⁸. As reported in ref.²⁸ the total computational time for the co-flow regime is below one second meaning that the counter-flow algorithm is also slower on the "per iteration" level. Partially responsible for this is the fact that ternary solution in the cathode requires more computation than binary solution assumed in ref.²⁸, however, in the major part this is simply the case of less efficient algorithm. The reason for this most probably lies with the program code being in its early development phase. This analysis thus indicates a potentially very large room for the computational algorithm optimisation towards shortening the computational times. Furthermore, the computational times of HAN model evaluated in this paper have a considerable margin for additional improvement by programming the model in a programming language such as C or Fortran that are more suitable for achieving short computational times than Mathematica and by executing the simulation on multiple CPU cores.

7. Conclusions

The paper presented an extended version of the Hybrid Analytic-Numerical fuel cell model (HAN) for a realistic straight parallel channel fuel cell from ref.²⁸, which efficiently combines three main features:

- 1D numerical treatment of gas flow,
- analytic 2D solution for the species concentration profile in the plane perpendicular to the gas flow and
- electrochemical sub-model.

the model extension presented in this paper makes the HAN model capable of addressing:

- ternary gas mixtures and
- counter-flow configuration

The 1D pipe flow + 2D concentration profile approach effectively make HAN a model with 3D resolution. The key to the hybrid 3D solution is in its construction in the form of a series of consecutive 2D analytic solutions that are obtained by dividing and solving the 2D diffusion problem on separate computational domains. This enables modelling of realistic fuel cell geometries and gives computationally efficient results with high accuracy. The efficient incorporation of the electrochemical

sub-model is owed to the derivative approximation and estimation-iteration approach.

Overall, HAN proves to be very accurate and computationally efficient with outlooks for reduction in computational times and is thus a very promising standalone fuel cell model for system level simulations. Further challenges in developing HAN for system level simulations remain the treatment of liquid water in GDLs and channels and non-straight channel geometries.

8. References

1. H. L. Hellman, R. van den Hoed, *Int. J. Hydrogen Energy*. 3, **2007**, 32, 305–315.
2. H. Ly, E. Birgersson, M. Vynnycky, *Int. J. Hydrogen Energy*. 9, **2012**, 37, 7779–7795.
3. K. Haraldsson, K. Wipke, *J. Power Sources*. 1–2, **2003**, 126, 88–97.
4. D. Cheddie, N. Munroe, *J. Power Sources*. 1–2, **2005**, 147, 72–84.
5. V. Gurau, J. A. Jr. Mann, *SIAM J. Appl. Math.* 2, **2009**, 70, 410–454.
6. M. U. Iftikhar et al., *J. Power Sources*. 2, **2006**, 160, 1170–1182.
7. R. Tirnovan et al., *Int. J. Hydrogen Energy*. 21, **2008**, 33, 6232–6238.
8. X. D. Xue, K. W. E. Cheng, D. Sutanto, *Electrochimica Acta*. 3, **2006**, 52, 1135–1144.
9. T. E. Springer, T. A. Zawodzinski, S. Gottesfeld, *J. Electrochem. Soc.* 8, **1991**, 138, 2334–2342.
10. M. Wöhr et al., *Int. J. Hydrogen Energy*. 3, **1998**, 23, 213–218.
11. G. Maggio, V. Recupero, L. Pino, *J. Power Sources*. 2, **2001**, 101, 275–286.
12. V. Gurau, F. Barbir, H. Liu, *J. Electrochem. Soc.* 7, **2000**, 147, 2468–2477.
13. J. J. Baschuk, L. Xianguo, *Applied Energy*. 2, **2009**, 86, 181–193.
14. B. P. M. Rajani, A. K. Kolar, *J. Power Sources*. 1, **2007**, 164, 210–221.
15. M. K. Baboli, M. J. Kermani, *Electrochimica Acta*. 26, **2008**, 53, 7644–7654.
16. H. Meng, *J. Power Sources*. 1, **2006**, 162, 426–435.
17. B. R. Sivertsen, N. Djilali, *J. Power Sources*. 1, **2005**, 141, 65–78.
18. M. A. R. S. Al-Baghdadi, *Proc. IMechE*. 6, **2008**, 222, 569–585.
19. Y. Wang, C. Wang, *J. Power Sources*. 1, **2006**, 153, 130–135.
20. A. Vath et al., *J. Power Sources*. 2, **2006**, 157, 816–827.
21. M. A. R. S. Al-Baghdadi, H. A. K. S. Al-Janabi, *Proc. IMechE*. 7, **2007**, 221, 917–929.
22. F. Muelleret al., *J. Power Sources*. 2, **2007**, 163, 814–829.
23. S. L. Ee, E. Birgersson, *J. Electrochem. Soc.* 10, **2011**, 158, 81224–81234.

24. G. Kim et al., *J. Power Sources*. 10, **2010**, 195, 3240–3249.
25. Q. Esmaili, A. A. Ranjbar, M. Abdollahzadeh, *International J. Green Energy*. 2, **2013**, 10, 190–204.
26. C. Y. Ling, S. L. Ee, E. Birgersson, *Electrochimica Acta*. 30, **2013**, 109, 305–315.
27. P. Chang et al., *J. Computational Physics*. 2, **2007**, 223, 797–821.
28. G. Tavčar, T. Katrašnik, *Energies*. 10, **2013**, 6, 5426–5485.
29. –, *J. Power Sources*. **2013**, 236, 321–340.
30. R. Timovan et al., *J. Power Sources*. 2, **2008**, 175, 773–778.
31. M. Hatti, M. Tioursi, *Int. J. Hydrogen Energy*. 11, **2009**, 34, 5015–5021.
32. S. Campanari, G. Manzolini, F. G. de la Iglesia, *J. Power Sources*. 2, **2009**, 186, 464–477.
33. R. M. Moore et al., *J. Power Sources*. 2, **2006**, 159, 1214–1230.
34. X. Xue et al., *J. Power Sources*. 2, **2004**, 133, 188–204.
35. C. Lee, J. Yang, *J. Power Sources*. 8, **2011**, 196, 3810–3823.
36. P. R. Pathapati, X. Xue, J. Tang, *Renewable Energy*. 1, **2005**, 30, 1–22.
37. R. M. Moore et al., *J. Power Sources*. 2, **2005**, 141, 272–285.
38. L. Boulon et al., *Renewable Energy*. **2012**, 46, 81–91.
39. Z. Lemeš et al., *J. Power Sources*. 2, **2006**, 154, 386–393.
40. M. Hinaje et al., *Energies*. 8, **2012**, 5, 2724–2744.
41. Z. Zhong, X. Zhu, G. Cao, *J. Power Sources*. 1, **2006**, 160, 293–298.
42. E. L. Cussler: Diffusion: mass transfer in fluid systems 3rd edition, Cambridge University Press, Cambridge, UK, **2009**, ISBN: 978-0-521-87121-1.
43. AVL LIST GmbH: AVL FIRE version 2011 Main Program, User Manual, Document No. 08.0201, Graz, **2011**.
44. B. Cockburn, G. Kanschat, D. Schötzau, *J. Sci. Comput.* 1–2, **2007**, 31, 61–73.
45. C. Fink, N. Fouquet, *Electrochimica Acta*. 28, **2011**, 56, 10820–10831.
46. N. Fouquet, C. Fink, R. Tatschl, 3D Modeling of PEM Fuel Cell with AVL FIRE: AVL Advanced Simulation Technologies International User Conference 2011, Graz, Austria, **2011**

Povzetek

Model gorivne celice PEM z ravnimi vzporednimi kanali predstavljen v tem članku razširja inovativni hibridni 3D analitično-numerični (HAN) pristop, predstavljen v predhodnih publikacijah istih avtorjev, z zmožnostma popisa tro-komponentnih plinskih zmesi in protitočnih geometrij. Jedro modela je princip modeliranja transporta snovi z 2D analitično rešitvijo za porazdelitev koncentracije snovi v ravnini pravokotni na smer toka plina v kanalu in sklapljanjem zaporednih takih 2D rešitev s pomočjo 1D numeričnega modela za tok plina po cevi. Elektrokemijska kinetika in drugi nelinearni procesi so s transportom snovi sklopljeni s pomočjo rutine odvodne aproksimacije v prediktivno-iterativni zanki. Slednje je tudi jedro protitočnega računskega algoritma. V članku je predstavljen model HAN laboratorijske testne gorivne celice in ovrednoten s primerjavo s profesionalnim 3D CFD simulacijskim orodjem. Rezultati predstavljenega modela HAN kažejo zelo dobro ujemanje z rezultati CFD simulacij. Model HAN doseže visoko natančne rezultate ob kratkih računskih časih, za kar sta zaslužna njegova delno analitična narava in učinkovita računska sklopitev elektrokemijske kinetike in transporta snovi.